Check for updates

Activation engineering on metallic 1T-MoS$_2$ by constructing *In-plane* heterostructure for efficient hydrogen generation

Zhipeng Liu [a], Kaiwen Wang [a], Yanjuan Li [b], Shisheng Yuan [a], Guoqing Huang [a], Xiaotian Li [a], Nan Li [a,*]

[a] *Key Laboratory of Automobile Materials (Ministry of Education), School of Materials Science and Engineering, Jilin University, 2699 Qianjin Street, Changchun 130012, PR China*
[b] *School of Chemistry and Materials Science, Jiangsu Normal University, Xuzhou 201116, PR China*

ARTICLE INFO

ABSTRACT

The metallic polymorph of molybdenum disulfide (1T-MoS$_2$) is a promising catalyst towards the hydrogen evolution reaction (HER). However, the intrinsic activity on basal plane is significantly inferior to that at edges despite the dominate number of basal plane atoms. Herein, we conducted an activation engineering to enhance the catalytic activity of the basal plane by constructing *in-plane* heterostructure with CoS$_2$ nanodomains embedded in 1T-MoS$_2$ basal plane (CoS$_2$@1T-MoS$_2$). Experimental and DFT analysis demonstrates a charge transfer from both CoS$_2$ and 1T-MoS$_2$ to the interface, which enables the formation of electron rich sites with high activity. Moreover, the *in-plane* heterostructure fully exposes the heterogeneous interfaces and promotes the accessibility of active sites. Consequently, the CoS$_2$@1T-MoS$_2$ delivers an excellent performance towards the HER with an overpotential of 72 mV at 10 mA·cm^{-2}, Tafel slope of 45 mV·dec^{-1} as well as remarkable stability. This work proposes a strategy to design highly efficient electrocatalysts based on 1T-MoS$_2$.

1. Introduction

The world prosperity is boosted by drastic depletion of fossil fuels, whereas the accompanied severe global environment deterioration and energy crisis arises extremely urgent to explore sustainable and clean energy [1,2]. Owing to the secure, renewable and high-efficiency features, hydrogen energy has been advocated as an appealing alternative for fossil fuels. Nevertheless, the application of hydrogen to serve as a predominant energy carrier that satisfy the growing globe energy demand can only be realized through its efficient, low cost and environmentally friendly production.[3] Among diverse feasible routes, water electrolysis, preferably driven by renewable electricity supply, is a desirable option with the advantages of readily available reactant, scalable device and highly-pure product, but it requires high-efficient electrocatalysts to accelerate the sluggish reaction process. From a prospective of practical application, developing efficient and scalable electrocatalysts is an essential prerequisite for an available future hydrogen economy [4,5].

In regard to the hydrogen evolution reaction (HER) through water electrolysis, molybdenum disulfide (MoS$_2$) is proposed as a competitive

catalyst. Typically, MoS$_2$ occurs in a layered structure similar to graphite, but individual layer is constructed by S-Mo-S sandwiched atoms. Depending on the atomic stacking configurations, MoS$_2$ can exist in different polymorphs, which exhibit distinct electrochemical properties [6]. The semiconducting phase MoS$_2$ polymorph (2H-MoS$_2$) is in a hexagonally packed structure, wherein the active sites are limited to the edges but the basal plane is electrochemical inert [7,8]. Another polymorph, i.e. the metallic phase (1T-MoS$_2$) that composed of edge-sharing MoS$_6$ octahedra exhibits catalytic activity on both the basal plane and the edges [9,10]. Moreover, the electronic conductivity of 1T-MoS$_2$ is approximately five ordered of magnitude higher than its 2H counterpart [11,12]. Both aspects make 1T-MoS$_2$ a more promising alternative catalyst for the HER. However, the catalytic performance of 1T-MoS$_2$ is still not desirable for practical application [13,14]. One of the primary issue is that the per-site catalytic activity on basal plane is significantly inferior to that on edges, whereas most atoms are exposed on the basal plane in such a layered structure [15–17].

Generally, an ideal catalytic activity towards the HER is based on both facile adsorption and desorption processes [18]. In 1T-MoS$_2$, the basal plane is covered by coordination saturated S atoms, which deliver

---

relatively weak chemisorption capability towards H [19,20]. Therefore, further activating basal plane is a rational approach to effectuating highly efficient 1T-MoS$_2$ based catalyst. Recent reports have demonstrated that alien atom doping and defect engineering are viable methods to improve the catalytic activity of MoS$_2$ basal plane [21–25]. Although the mechanism involved are different, the catalytic activity enhancement is intrinsically based on modulation of local electronic structure of S atoms. Herein, we propose an appealing strategy to tailor local electronic structure of S atoms by constructing a heterostructure between 1T-MoS$_2$ and another transition metal sulfide. This kind of heterostructure has the following advantages: 1) the two sulfides tend to form intimate connect and share "S bridge" atoms at heterogeneous interfaces, thereby altering the coordinate state of S atoms; 2) an electron transfer at the heterogeneous interfaces can be expected as the metal atoms coordinated to interfacial S atoms are of different electronegativity [26,27]. Both aspects are desirable to modulate the electronic structure of S atoms on 1T-MoS$_2$ basal plane.

Based on the above analysis, we conducted an activation engineering on the basal plane of 1T-MoS$_2$ by embedding CoS$_2$ nanodomains in the basal plane of 1T-MoS$_2$ to construct an *in-plane* heterostrcture. Such an *in-plane* heterostructure created substantial interfacial S atoms coordinated with both Co and Mo atoms. The tailoring in coordination state modulates electronic structure of interfacial S atoms and enhances catalytic activity. Moreover, compared with the *out-plane* architecture with CoS$_2$ stacked on MoS$_2$, such an *in-plane* heterostructure can avoid coverage of the active interfaces. With these merits, the *in-plane* heterostructure (CoS$_2$@1T-MoS$_2$) exhibited remarkable performance towards the HER. The origin of such excellent activity was further revealed based on DFT calculation.

2. Experimental section

2.1. Material preparation

2.1.1. Preparation of Co-precursor nanowire array

The Co-precursor [Co(OH)$_x$(CoO$_3$)$_y$·nH$_2$O] nanowire array was synthesized on carbon cloth via a conventional hydrothermal procedure. Typically, 0.69 g of cobalt nitrate hexahydrate (Co(NO$_3$)·6H$_2$O) and 0.72 g of urea ((NH$_2$)$_2$CO) were dissolved in 24 mL solution of distilled water and ethanol (volume ratio of 1:1). Then the solution was transferred into a Teflon lined-stainless steel autoclave. A piece of carbon fiber cloth (2 × 3 cm^2), rinsed subsequently with 3 M hydrochloric acid, distilled water and ethanol was emerged in the above solution. The autoclave was sealed and heated in an oven at 95 ºC for 6 h. After cooling, the carbon fiber cloth was removed, rinsed with distilled water and dried in air.

2.1.2. Preparation of CoS$_2$@1T-MoS$_2$

CoS$_2$@1T-MoS$_2$ was obtained in a one-step hydrothermal process with [Co(OH)$_x$(CoO$_3$)$_y$·nH$_2$O] nanowire array as a self-sacrifice template. First, 6 mg molybdenum trioxide (MoO$_3$) and 100 mg sodium sulfide (Na$_2$S·9H$_2$O) were dissolved in 24 mL distilled water to form a yellow solution under stirring. Subsequently, 30 mg thioacetamide (TAA) and 120 mg urea ((NH$_2$)$_2$CO) were added and the solution was stirred for 10 mins before transferred into an autoclave. The as-obtained Co-precursor nanowire array on carbon cloth (2 × 3 cm^{-2}) was submerged in the solution and the autoclave was sealed and heated at 200 ºC for 12 h. After natural cooling, the carbon fiber cloth was fetched and rinsed with water, ethanol and carbon disulfide to eliminate residues.

2.1.3. Preparation of 1T-MoS$_2$-NS, CoS$_2$-MW and CoS$_2$/1T-MoS$_2$

1T-MoS$_2$-NS was prepared via a one-step hydrothermal method. First, 6 mg molybdenum trioxide (MoO$_3$) and 100 mg sodium sulfide (Na$_2$S·9H$_2$O) were dissolved in 24 mL distilled water to form a yellow solution under stirring. Subsequently, 30 mg thioacetamide (TAA) and 120 mg urea ((NH$_2$)$_2$CO) were added and the solution was stirred for 10

mins before transferred into an autoclave. A piece of carbon cloth (2 × 3 cm^{-2}) was submerged in the solution and the autoclave was sealed and heated at 200 ºC for 12 h. After natural cooling, the carbon fiber cloth was fetched and rinsed with water, ethanol and carbon disulfide to eliminate residues. The CoS$_2$-NW was obtained via a one-step hydrothermal synthesis. Firstly, Co-precursor nanowire array was submerged in 24 mL aqueous solution containing 300 mg Na$_2$S·9H$_2$O before transferred into an autoclave. The autoclave was sealed and heated at 200 ºC for 12 h. The CoS$_2$/1T-MoS$_2$ sample was synthesized via a route similar to that CoS$_2$@1T-MoS$_2$ but the as-obtained CoS$_2$ nanowire array instead of Co(OH)$_x$(CoO$_3$)$_y$·nH$_2$O nanowire array was served as a template.

2.2. Characterization

X-ray diffraction (XRD) was performed using a DX2700 X-ray diffractometer with a Cu Kα radiation source (λ = 0.15406 nm). X-ray photoelectron spectra (XPS) were obtained from a ESCALAB 250 electron spectrometer with an Al Kα radiation source (h·ν = 1486.6 eV). The microstructures of the samples were studied under a scanning electron microscope (SEM; JEOL JSM-6700F) at 10 kV of acceleration voltage and a transmission electron microscope (TEM; JEOL JEM-2100F) at 200 kV of acceleration voltage. High-angle annular dark-field imaging scanning transmission electron microscopy (HADDF-STEM) was obtained on a FEI Themis Z spherical aberration electron microscope at 200 kV acceleration voltage. Energy dispersive X-ray (EDX) data were collected using an INCA-EDX electron energy dispersive spectroscope.

2.3. Electrochemical measurement

Electrochemical tests were performed with a three-electrode system by using a CHI650E electrochemical workstation in an N$_2$-saturated 0.5 M H$_2$SO$_4$ or 1 M KOH aqueous solution. The sample with self-supporting structure was directly applied as working electrode. A graphite rod was used as the counter electrode, and a saturated Hg/HgCl$_2$ and a Hg/HgO electrode was served as a reference electrode in acid or alkaline condition, respectively.

Linear sweeping voltammetry (LSV) measurements were conducted from 0 to − 0.6 V versus a reversible hydrogen electrode (RHE) at a scan rate of 2 mV·s^{-1}. Tafel slopes were derived from LSV curves by fitting the data into the Tafel equation: η = a + b·log j. In the equation, η is the overpotential, j is the corresponding current density, and b is the Tafel slope. Cyclic voltammetry (CV) measurements were recorded from 0.1 to 0.3 V versus RHE at a series of scan rates from 20 to 180 mV·s^{-1} with 20 mV intervals. Chronoamperometry curve was recorded at a static potential of 100 mV and electrochemical stability was tested by conducting CV 1000 times between 0 and − 0.6 V.

2.4. Calculation Details

All the calculations were performed on the basis of the DFT methods implemented in the Vienna Ab initio Simulation Package (VASP 5.4.4). The generalized gradient approximation was used to estimate exchange–correlation interaction in the scheme of the Perdew–Burke–Ernzerhof functional.4 The effect of core electrons on the density of valence electrons was described using the projector augmented wave method. The kinetic energy cutoff for the plane waves was set to 450 eV for all the calculations. The convergence tolerance of energy and force on each atom during structure relaxation were less than 10^{-5} eV and 0.03 eV/Å, respectively. A set of Monkhorst–Pack mesh K points of 3 × 3 × 1 and 5 × 5 × 1 were used to sample the Brillouin zone for geometry optimization and electronic structural calculations. A vacuum distance of 20 Å was set to ensure sufficient vacuum and avoid interactions between two periods.

The HER catalytic activity of materials can be evaluated by ΔG$_H$, which is defined as.

$$\Delta G_H = \Delta E_H + \Delta E_{ZPE} - T\Delta S_H,$$

where ΔE_H is the hydrogen adsorption energy defined as.

$$\Delta E_H = E_{(System+\ H)} - E_{(System)} - 1/2\ E_{H2},$$

in which $E_{(System+\ H)}$ and $E_{(System)}$ are the energies of all research systems with and without H adsorption, respectively. ΔE_{ZPE} is the amount of change of zero-point energy in the total system, and T is 300 K. ΔS_H is the entropy change of the H atom after it transits from gaseous to adsorbed state. Herein, $\Delta E_{ZPE} - T\Delta S_H$ is approximated to 0.24. See more details in the supporting information.

3. Result and discussion

3.1. Structural and morphology analysis

The *in-plane* heterostructure of CoS_2 and $1T\text{-}MoS_2$ was fabricated via a self-sacrificing template method as illustrated in Fig. 1. Nanowire array of $Co(OH)_x(CO_3)_y \cdot nH_2O$ (Fig. S1) was utilized as Co precursor as well as a template. Through a hydrothermal sulfurization synthesis, MoS_2 nanosheets grew on the nanowires and the nanowires gradually vanished, leaving hollow tabular architecture as shown in scanning electron microscopy (SEM, Fig. 2a) and transmission electron microscopy (TEM, Fig. 2b) images. Each individual tube is approximately 100 nm in diameter and 1 μm in length, constructed with multilayered MoS_2 nanosheets. Energy dispersive X-ray (EDX) elemental mapping (Figs. 2c and S2) manifests that Co, Mo and S elements are uniformly distributed along the nanosheets, which indicates that the internal Co species in the nanowire template are completely dissolved and CoS_2 is well dispersed on the $1T\text{-}MoS_2$ nanosheets.

It is worth of noting that the $Co(OH)_x(CO_3)_y \cdot nH_2O$ nanowires gradually dissolve and releases Co species slowly, which tend to form ultrasmall CoS_2 domains (Fig. S3, S4). These CoS_2 domains can be accommodated at the defect regions in MoS_2 basal plane, bonding to MoS_2 through S bridges and forming an *in-plane* heterostructure. According to the DFT calculation (Fig. S5), the cohesive energy of such an *in-plane* heterostructure (-5.1 eV) is significantly lower than that of the *out-plane* heterostructure (-4.5 eV), indicating the *in-plane* heterostructure is thermodynamically more favorable. In validation of such an *in-plane* heterostructure, the constitution of individual nanosheet was inspected by high resolution transmission electron microscopy (HRTEM and HADDF-STEM). Representative images of the basal plane of the nanosheet are presented in Figs. 2d and S2, which reveal distinct lattice patterns. The lattice observed in the region marked with blue rectangle reveals an interplanar space of 0.27 nm, corresponding to (100) plane of 1 T phase MoS_2 with tetragonal symmetry of atomic arrangement [6,28,29]. In contrast, the region marked with green rectangle displays fringes with a distance of 0.24 nm that correlated with (210) plane of CoS_2 [30]. The nanodomains of CoS_2 was found in diameter of 2 nm with clear boundary (labeled by red lines) shared with the $1T\text{-}MoS_2$ lattice regions. Additionally, the HADD-STEM reveals lattices in similar contrast (insert in Fig. 2b). The above observations manifest the formation of *in-plane* heterostructure.

Phasic and chemical compositions of the heterostructure was investigated via Raman and X-ray photoelectron spectroscopy (XPS). The Raman spectrum (Fig. 3a) of $CoS_2@1T\text{-}MoS_2$ reveals peaks corresponds to $E_{1\,g}$ (280 cm^{-1}), $E^1_{2\,g}$ (350 cm^{-1}) and $A_{1\,g}$ (404 cm^{-1}) vibrational modes in MoS_2. While the other three peaks occur at 145, 210 and 330 cm^{-1} are attributed to J_1, J_2 and J_3 vibrational modes, which are characteristic of $1T\text{-}MoS_2$ [9,12]. Furthermore, X-ray photoelectron spectra (XPS) demonstrate an electron transfer between CoS_2 and $1T\text{-}MoS1T\text{-}MoS1T\text{-}MoS_2$. Herein, samples with mono-component i.e., $1T\text{-}MoS_2$ nanosheets ($1T\text{-}MoS_2\text{-}NS$) and CoS_2 nanowires ($CoS_2\text{-}NW$) were prepared as references (see morphology in Fig. S6). The pristine $CoS_2\text{-}NW$ delivers a doublet at 794.3 eV ($2p_{3/2}$) and 779.1 eV ($2p_{1/2}$) in Co 2p spectrum (Fig. 3b), which is ascribed to Co^{2+} species in CoS_2 [31]. The accompanied peaks are attributed to satellite peaks. By contrast, in $CoS_2@1T\text{-}MoS_2$ the Co species was found in a binding energy 0.9 eV higher than that of pristine $CoS_2\text{-}NW$. Moreover, in Mo 3d spectra, a chemical shift is also observed comparing $CoS_2@1T\text{-}MoS_2$ and $1T\text{-}MoS_2\text{-}NS$ (Fig. 3c). Pristine $1T\text{-}MoS_2\text{-}NS$ reveals a conspicuous doublet at 231.6 eV ($3d_{5/2}$) and 228.4 eV ($3d3_{/2}$) in Mo 3d spectrum, corresponding to Mo^{4+} species in $1T\text{-}MoS_2$ [32,33]. By comparison, in $CoS_2@1T\text{-}MoS_2$ the identical doublet occurs with slightly higher binding energy (0.2 eV). These results indicate an electron depletion from both Mo and Co atoms in $CoS_2@1T\text{-}MoS_2$. In S 2p spectrum, $CoS_2@1T\text{-}MoS_2$ delivers a predominant doublet at 162.2 and 161.4 eV, which is consistent with S^{2-} species in pristine $1T\text{-}MoS_2$ [33,34]. Whereas the other weak doublet found at 163.5 and 162.7 eV is in binding energy higher than that of $1T\text{-}MoS_2\text{-}NS$ but significantly lower than that of $CoS_2\text{-}NW$. This doublet probably corresponds to S species coordinated with both Co and Mo atoms at the heterogeneous interfaces, which is in chemical state distinct to pristine CoS_2 and $1T\text{-}MoS_2$. A hybrid sample with similar components but constructed with $1T\text{-}MoS_2$ coated on CoS_2 nanowires (denoted as $CoS_2/1T\text{-}MoS_2$, see morphology in Fig. S6) is involved for comparison. Notably, this core-shell structure of $CoS_2/1T\text{-}MoS_2$ contains negligible heterogeneous interfaces. The
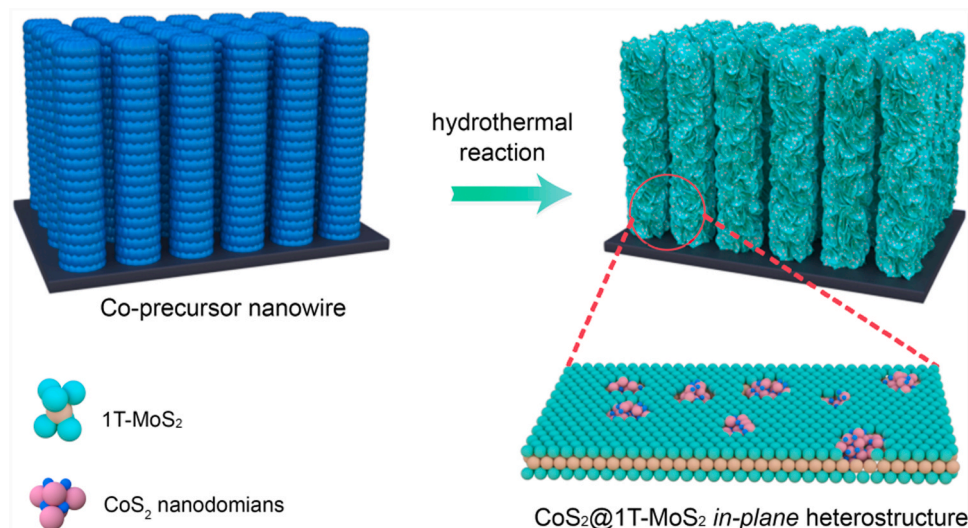

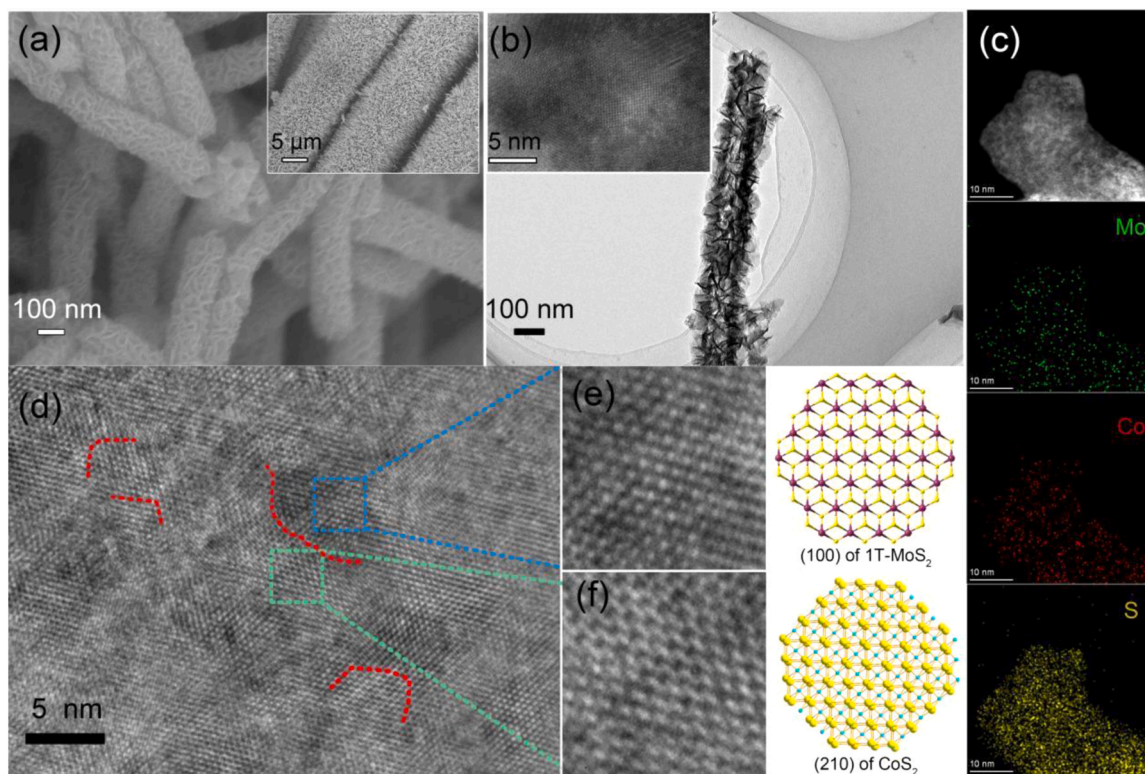**Fig. 1.** Schematic of synthesis process of $CoS_2@1T\text{-}MoS_2$.

Fig. 2. (a) SEM, (b) TEM image (insert HADDF image) and (c) STEM-EDX elemental mapping of $CoS_2@1T-MoS_2$; (d) HRTEM image on the basal plane of $CoS_2@1T-MoS_2$ and (e, f) zoom-in view of the selected regions and corresponding lattice schematic.

corresponding S spectrum of $CoS_2/1T-MoS_2$ delivers doublets consistent with pristine $1T-MoS_2$ and CoS_2 respectively (Fig. S7), indicating there is negligible electron transfer between the two components. Therefore, the distinct S spectrum of $CoS_2@1T-MoS_2$ compared with $CoS_2/1T-MoS_2$ indicates that the *in-plane* heterostructure induces electron transfer from Mo and Co atoms to the S atoms at heterogeneous interfaces, which consequently alters the intrinsic electronic structure.

3.2. Electrochemical performance

Electrocatalytic activity of $CoS_2@1T-MoS_2$ towards the HER was evaluated in Ar-saturated 0.5 M H_2SO_4 aqueous solution with a linear sweep voltammetry (LSV) measurement, where the self-supported electrode was directly applied as working electrode. Polarization curves presented in Fig. 3a reveal a remarkable activity of $CoS_2@1T-MoS_2$ towards the HER with a negligible onset potential and a small overpotential (η_{10}) of 72 mV to achieve a current density of 10 mA·cm^{-2}. Such performance is obviously enhanced compared with CoS_2-NW (η_{10} = 321 mV) and $1T-MoS_2$-NS (η_{10} = 258 mV). In addition, the $CoS_2@1T-MoS_2$ outperforms the hybrid $CoS_2/1T-MoS_2$ (η_{10} = 171 mV) electrode, which demonstrate that heterogeneous interfaces formed in the $CoS_2@1T-MoS_2$ *in-plane* heterostructure provide superior catalytic activity.

Generally, in acidic condition the HER proceeds by multistep reactions following two possible mechanisms that involves adsorption and desorption of H* species, i.e. Volmer-Heyrovsky and Vomler-Tafel mechanism [35]. To reveal HER mechanism, we derived Tafel plots of the samples respectively from polarization curves. As depicted in Fig. 3b, $CoS_2@1T-MoS_2$ displays a Tafel slope of 45 mV·dec^{-1}, indicating the HER predominantly follows the Volmer-Heyrovsky mechanism. Compared with CoS_2-NW (77 mV·dec^{-1}), $1T-MoS_2$-NS (157 mV·dec^{-1}) and $CoS_2/1T-MoS_2$ (95 mV·dec^{-1}), the kinetic is obviously accelerated. The activity evaluated by Tafel slope and overpotential of $CoS_2@1TCoS_2@1T-MoS_2$ is plotted with other

recently-reported MoS_2 based electrocatalysts (the electrochemical data are listed in Table S1). The diagram (Fig. 3c) suggests the catalytic activity of $CoS_2@1T-MoS_2$ is quite competitive among the MoS_2-based catalysts.

In addition, $CoS_2@1T-MoS_2$ exhibits remarkable cycling stability. The LSV curves measured on $CoS_2@1T-MoS_2$ before and after 1000 CV cycles are presented in Fig. 4d, which shows negligible decay in current density. A chronoamperometry measurement under a constant overpotential reveals stable H_2 generation for at least 40 h. Moreover, $CoS_2@1T-MoS_2$ also exhibits a remarkable activity and stability toward the HER in alkaline condition with a η_{10} = 114 mV (Fig. 3f and Fig. S8) [36,37].

3.2.1. DFT calculation

We further conducted density functional theory (DFT) calculation to reveal the mechanism underlying the significantly enhanced HER activity of $CoS_2@1T-MoS_2$. The calculation model was constructed on the basis of experimental observations, wherein CoS_2 was embedded in the lattice of $1T-MoS_2$ and the two components share S atoms at the heterogeneous interfaces (the corresponding structure is illustrated in Fig. S8a, b). Deformation charge density diagram (Fig. 4a, Fig. S8c, d) demonstrates an uneven distribution of electrons in the heterostructure, where charge accumulation region mainly occurs around the S atoms at heterogeneous interfaces (represented by purple region), while charge depletion is found at the metal sites (represented by green region). This result is in accordance with the XPS analysis that electrons transfer from both CoS_2 and $1T-MoS_2$ bulk lattices to the heterogeneous interfaces. Consequently, the electron density of S atoms at the heterogeneous interfaces that coordinated with both Co and Mo atoms is significantly increased.

Typically, the hydrogen absorption free energy (ΔG_H) is applied as a descriptor for the intrinsic catalytic activity for a HER catalyst, wherein an ideal activity is achieved as ΔG_H approaching 0 eV [16,38]. In the case of pristine $1T-MoS_2$, only S atoms are exposed on basal plane
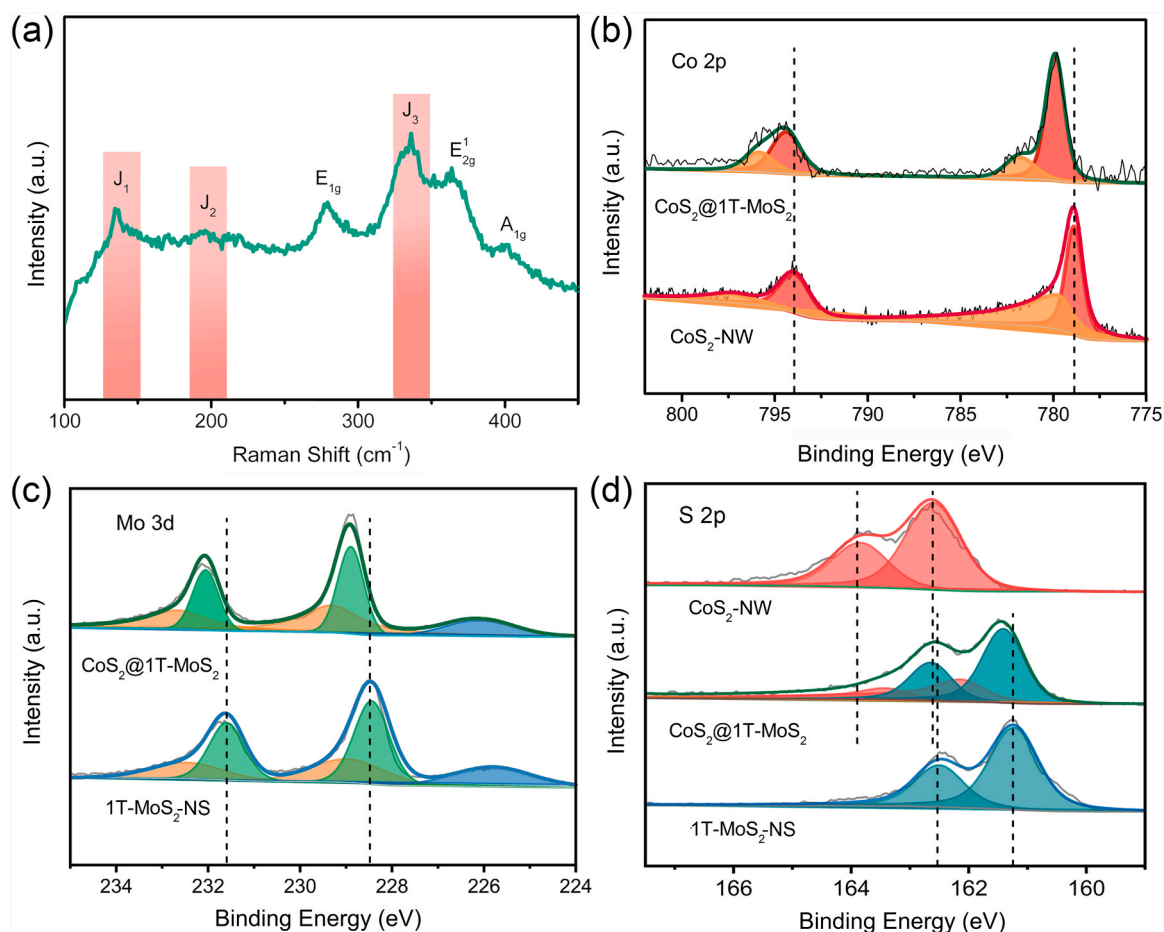
Fig. 3. (a) Raman spectrum of CoS$_2$@1T-MoS$_2$. (b-d) Co 2p, Mo 3d and S 2p XP spectra of CoS$_2$@1T-MoS$_2$, CoS$_2$-NW and 1T-MoS$_2$-NS.
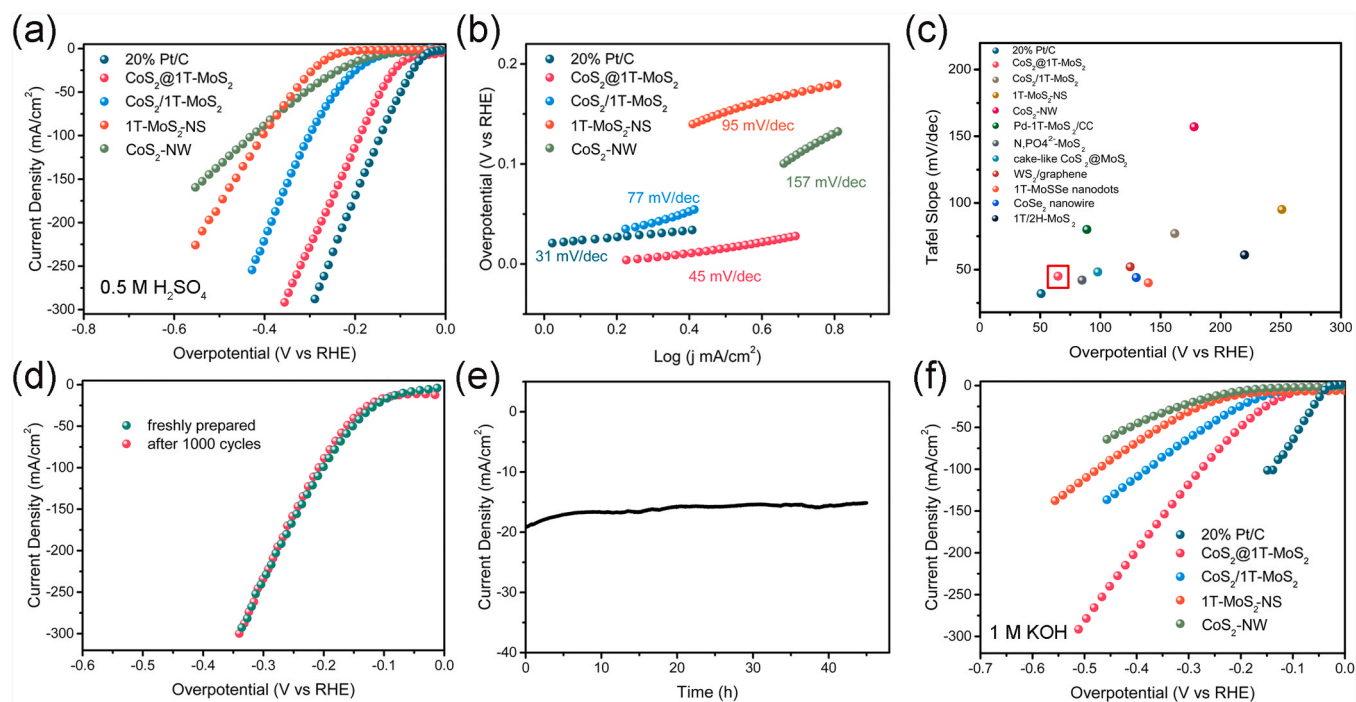

Fig. 4. Electrochemical performance of CoS$_2$@1T-MoS$_2$ and reference samples. (a) LSV curves in acid (0.5 M H$_2$SO$_4$), (b) corresponding Tafel slopes, (c) a comparison of HER activity of the reported MoS$_2$-based catalysts with Tafel slopes (mV·dec^{-1}) vs. overpotential at 10 mA·cm^{-2}, (d) LSV curves of CoS$_2$@1T-MoS$_2$ before and after 1000 CV cycles, (e) i-t curve under constant overpotential and (f) LSV curves in alkaline condition (1 M KOH).

(denoted as BS). For these S sites, a $\Delta G_H = 0.98$ eV was calculated (Fig. 4b), indicating a weak chemisorption capability towards H [19,20]. By contrast, the ΔG_H drops to 0.45 eV (S1) and 0.60 eV (S2) for two representative S sites at heterogeneous interfaces respectively (the co-ordination state was depicted in Fig. 6c). It reveals the electron accumulation at the heterogeneous interface enhances adsorption capability of S atoms towards H, which consequently promotes the intrinsic catalytic activity.

The electronic states of the S atoms at heterogeneous interfaces were inspected to further elucidate the correlation between the charge transfer in the *in-plane* heterostructure and the enhanced adsorption capability. The projected density of electronic states (pDOS) of BS, S1 and S2 are displayed in Fig. 5a. When a H atom interacts with an active S atom, the 1s orbital of the H atom strongly hybridizes with the 2p orbital of S atom, forming a fully filled σ bond with lower energy and an antibond (σ*) with relatively higher energy (Fig. 5a) [39,40]. For S1 and S2, the σ bonding center occurs at relatively higher energy state than that of BS. The higher position of σ center indicates an increase in the filling of the covalent σ orbital by electrons and lower occupancy of σ*, which consequently leads to a stronger bonding between H and S atoms.[41] Furthermore, the bonding strength between H atoms and the afore-mentioned S sites were quantified by the crystal orbital Hamilton population (COHP). The bonding (COHP > 0) and antibonding (COHP < 0) interactions of H adsorbed on various S sites are presented in Fig. 6c, wherein the bonding states of S1 and S2 are found in obviously deeper states than that on pristine basal plane. The corresponding integrated COHP value (ICOHP) up to Fermi level for S1, S2 and BS was calculated as − 5.38 eV, − 5.28 eV and − 2.75 eV respectively, which reveals that the interaction strength is dramatically enhanced on S atoms at the heterogeneous interfaces [42,43] The aforementioned analysis indicates electron modulation significantly promotes the adsorption capability of interfacial S atoms towards H atoms, thereby enhancing the intrinsic catalytic activity. Moreover, unlike *out-plane* structure where the heterogeneous interfaces is easily shielded by the alien components, the *in-plane* heterostructure was constructed with CoS₂ cluster embedded in the basal plane of 1T-MoS₂ nanosheets, which is beneficial to expose substantial interfaces. In this regard, the remarkable catalytic activity is based on the synergetic effect of electronic modulation and structure advantage.

4. Conclusion

An *in-plane* heterostructure was constructed with CoS₂ nanodomains embedded in the basal plane of 1T-MoS₂ nanosheet. Experimental and calculation analysis demonstrates an electron transfer from both 1T-MoS₂ and CoS₂ lattice to the heterogeneous interfaces, which increases the electron density of the interfacial S atoms. Such a change in electron density significantly enhances the adsorption capability of interfacial S atoms towards hydrogen and thus promotes the intrinsic catalytic activity. In addition, the *in-plane* structure fully exposes the heterogeneous interfaces. On the basis of the synergistic effect of electronic modulation and structure optimization, the as-obtained in-plane CoS₂@1T-MoS₂ heterostructure delivers a remarkable performance towards the HER with a small overpotential and robust stability both in acidic and alkaline condition.

CRediT authorship contribution statement

Zhipeng Liu: Data curation, Visualization, Methodology, Writing – original draft. **Kaiwen Wang:** Data curation, Visualization, Methodology. **Yanjuan Li:** Data curation, Visualization, Methodology. **Shisheng Yuan:** Data curation, Visualization, Methodology. **Guoqing Huang:**
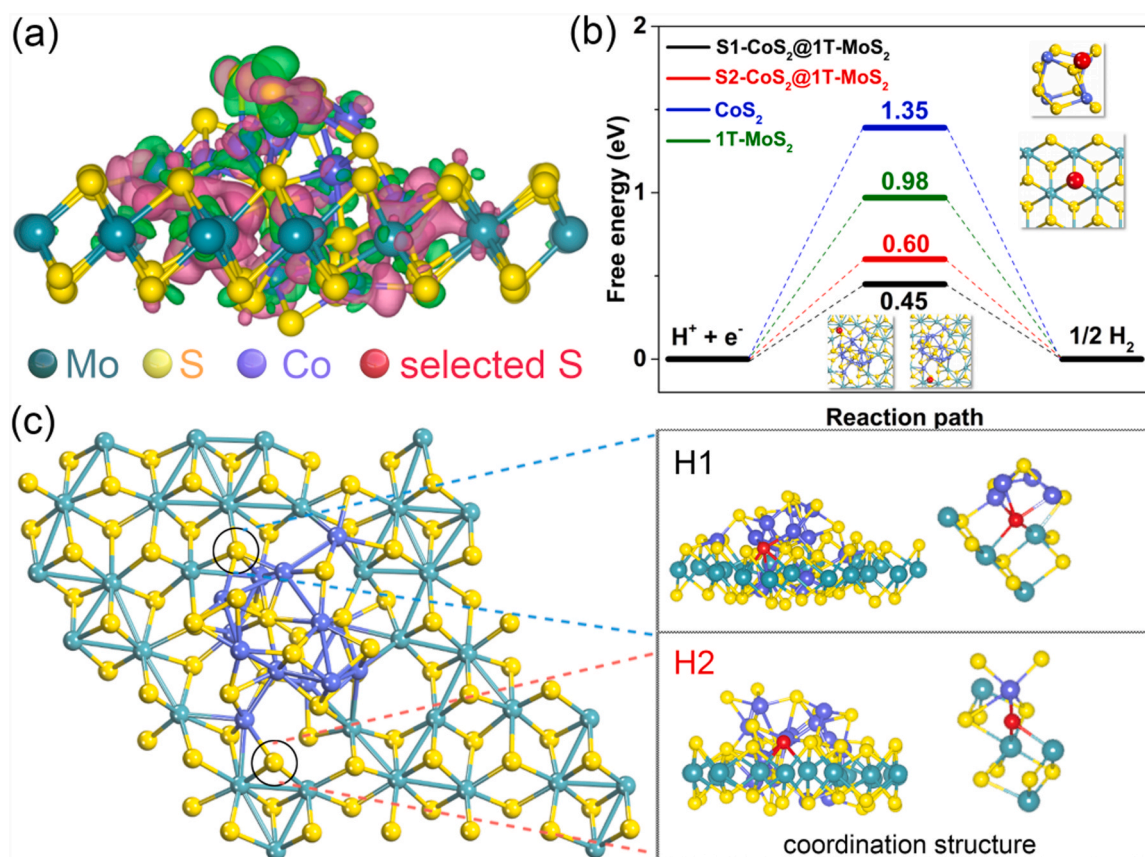
Fig. 5. (a) deformation charge density of CoS₂@1T-MoS₂ heterostructure. (b) Hydrogen absorption free-energy (ΔG_H) diagram of S atoms in CoS₂, on basal plane of 1T-MoS₂ and at heterogeneous interfaces (S1 and S2). (c) Schematic of coordination state of S1 and S2.
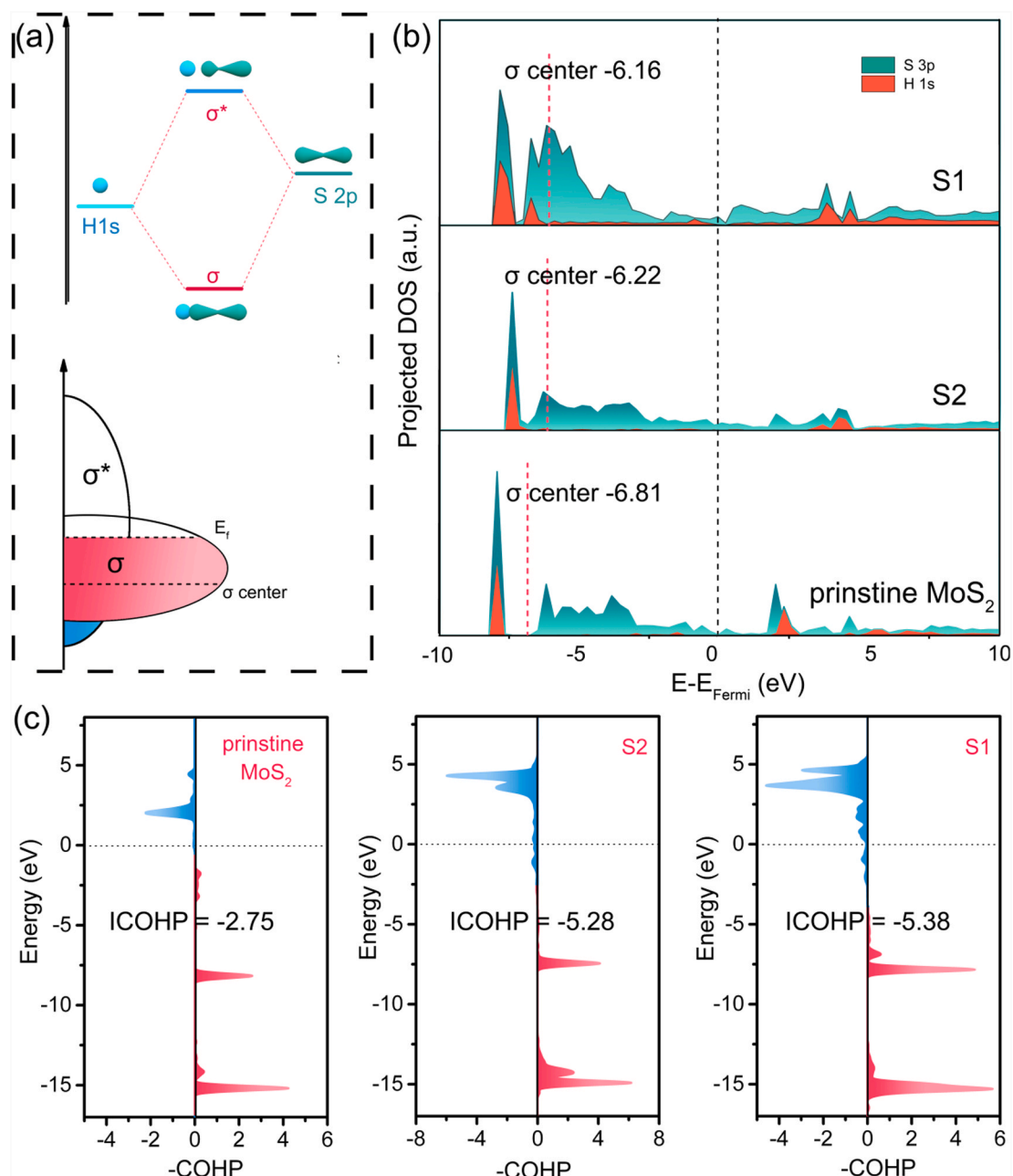
Fig. 6. (a) schematic of bonding state between S and H atoms. (b) pDOS diagram of the CoS_2@1T-MoS_2 heterostructure. (c) COHP profiles of CoS_2@1T-MoS_2 heterostructure.

Data curation, Visualization, Methodology. **Xiaotian Li:** Conceptualization, Funding acquisition, Supervision, Writing – review & editing. **Nan Li:** Conceptualization, Funding acquisition, Supervision, Writing – review & editing.

Declaration of Competing Interest

The authors declare that they have no known competing financial interests or personal relationships that could have appeared to influence the work reported in this paper.

Appendix A. Supporting information

Supplementary data associated with this article can be found in the online version at doi:10.1016/j.apcatb.2021.120696.

References

[1] J. Kibsgaard, Z. Chen, B.N. Reinecke, T.F. Jaramillo, Engineering the surface structure of MoS2 to preferentially expose active edge sites for electrocatalysis 11 (2012) 963–969.
[2] J. Zhu, L. Hu, P. Zhao, L.Y.S. Lee, K.Y. Wong, Recent advances in electrocatalytic hydrogen evolution using nanoparticles 120 (2020) 851–918.
[3] P.D. Luna, C. Hahn, D. Higgins, S.A. Jaffer, T.F. Jaramillo, E.H. Sargent, What would it take for renewably powered electrosynthesis to displace petrochemical processes? 364 (2019), eaav3506.
[4] W.-J. Jiang, T. Tang, Y. Zhang, J.-S. Hu, Synergistic modulation of non-precious-metal electrocatalysts for advanced water splitting 53 (2020) 1111–1123.

[5] Y. Li, Y. Sun, Y. Qin, W. Zhang, L. Wang, M. Luo, H. Yang, S. Guo, Recent advances on water-splitting electrocatalysis mediated by noble-metal-based nanostructured materials 10 (2020), 1903120.

[6] Y.C. Lin, D.O. Dumcenco, Y.S. Huang, K. Suenaga, Atomic mechanism of the semiconducting-to-metallic phase transition in single-layered MoS2 9 (2014) 391–396.

[7] T.F. Jaramillo, K.P. Jørgensen, J. Bonde, J.H. Nielsen, S. Horch, I. Chorkendorff, Identification of active edge sites for electrochemical H2 evolution from MoS2 nanocatalysts 317 (2006) 100–102.

[8] B. Hinnemann, P.G. Moses, J. Bonde, K.P. Jørgensen, J.H. Nielsen, S. Horch, I. Chorkendorff, J.K. Nørskov, Biomimetic hydrogen evolution: MoS2 nanoparticles as catalyst for hydrogen evolution 127 (2005) 5308–5309.

[9] R. Lv, J.A. Robinson, R.E. Schaak, D. Sun, Y.F. Sun, T.E. Mallouk, M. Terrones, Transition metal dichalcogenides and beyond: synthesis, properties, and applications of single- and few-layer nanosheets 48 (2015) 56–64.

[10] D. Voiry, M. Salehi, R. Silva, T. Fujita, M. Chen, T. Asefa, V.B. Shenoy, G. Eda, M. Chhowalla, Conducting MoS2 nanosheets as catalysts for hydrogen evolution reaction 13 (2013) 6222–6227.

[11] M. Acerce, D. Voiry, M. Chhowalla, Metallic 1T phase MoS2 nanosheets as supercapacitor electrode materials 10 (2015) 313–318.

[12] M. Chhowalla, H.S. Shin, G. Eda, L.-J. Li, K.P. Loh, H. Zhang, The chemistry of two-dimensional layered transition metal dichalcogenide nanosheets 5 (2013) 263–275.

[13] L. Li, P. Wang, Q. Shao, X. Huang, Metallic nanostructures with low dimensionality for electrochemical water splitting 49 (2020) 3072–3106.

[14] Y. Jiao, A.M. Hafez, D. Cao, A. Mukhopadhyay, Y. Ma, H. Zhu, Metallic MoS2 for high performance energy storage and energy conversion 14 (2018), 1800640.

[15] J. Zhang, J. Wu, H. Guo, W. Chen, J. Yuan, U. Martinez, G. Gupta, A. Mohite, P. M. Ajayan, J. Lou, Unveiling active sites for the hydrogen evolution reaction on monolayer MoS2 29 (2017).

[16] Y. Zang, S. Niu, Y. Wu, X. Zheng, J. Cai, J. Ye, Y. Xie, Y. Liu, J. Zhou, J. Zhu, X. Liu, G. Wang, Y. Qian, Tuning orbital orientation endows molybdenum disulfide with exceptional alkaline hydrogen evolution capability 10 (2019) 1217.

[17] B. Pattengale, Y. Huang, X. Yan, S. Yang, S. Younan, W. Hu, Z. Li, S. Lee, X. Pan, J. Gu, J. Huang, Dynamic evolution and reversibility of single-atom Ni(II) active site in 1T-MoS2 electrocatalysts for hydrogen evolution 11 (2020) 4114.

[18] Z.W. Seh, J. Kibsgaard, C.F. Dickens, I. Chorkendorff, J.K. Nørskov, T.F. Jaramillo, Combining theory and experiment in electrocatalysis: insights into materials design 355 (2017).

[19] N.H. Attanayake, A.C. Thenuwara, A. Patra, Y.V. Aulin, T.M. Tran, H. Chakraborty, E. Borguet, M.L. Klein, J.P. Perdew, D.R. Strongin, Effect of intercalated metals on the electrocatalytic activity of 1T-MoS2 for the hydrogen evolution reaction 3 (2017) 7–13.

[20] T. Zhang, H. Zhu, C. Guo, S. Cao, C.-M.L. Wu, Z. Wang, X. Lu, Theoretical investigation on the hydrogen evolution reaction mechanism at MoS2 heterostructures: the essential role of the 1T/2H phase interface 10 (2020) 458–465.

[21] J. Zhu, Z.C. Wang, H. Dai, Q. Wang, R. Yang, H. Yu, M. Liao, J. Zhang, W. Chen, Z. Wei, N. Li, L. Du, D. Shi, W. Wang, L. Zhang, Y. Jiang, G. Zhang, Boundary activated hydrogen evolution reaction on monolayer MoS2 10 (2019) 1348.

[22] Z. Luo, Y. Ouyang, H. Zhang, M. Xiao, J. Ge, Z. Jiang, J. Wang, D. Tang, X. Cao, C. Liu, W. Xing, Chemically activating MoS2 via spontaneous atomic palladium interfacial doping towards efficient hydrogen evolution 9 (2018) 2120.

[23] K. Qi, X. Cui, L. Gu, S. Yu, X. Fan, M. Luo, S. Xu, N. Li, L. Zheng, Q. Zhang, J. Ma, Y. Gong, F. Lv, K. Wang, H. Huang, W. Zhang, S. Guo, W. Zheng, P. Liu, Single-atom cobalt array bound to distorted 1T MoS2 with ensemble effect for hydrogen evolution catalysis 10 (2019) 5231.

[24] C. Tsai, H. Li, S. Park, J. Park, H.S. Han, J.K. Norskov, X. Zheng, F. Abild-Pedersen, Electrochemical generation of sulfur vacancies in the basal plane of MoS2 for hydrogen evolution, Nat. Commun. 8 (2017) 15113.

[25] H. Li, C. Tsai, A.L. Koh, L. Cai, A.W. Contryman, A.H. Fragapane, J. Zhao, H.S. Han, H.C. Manoharan, F. Abild-Pedersen, J.K. Nørskov, X. Zheng, Activating and optimizing MoS2 basal planes for hydrogen evolution through the formation of strained sulphur vacancies 15 (2016), 364-364.

[26] G. Zhao, K. Rui, S.X. Dou, W. Sun, Heterostructures for electrochemical hydrogen evolution reaction: a review 28 (2018), 1803291.

[27] H. Wang, W. Fu, X. Yang, Z. Huang, J. Li, H. Zhang, Y. Wang, Recent advancements in heterostructured interface engineering for hydrogen evolution reaction electrocatalysis 8 (2020) 6926–6956.

[28] M. Acerce, D. Voriy, M. Chhowalla, Metallic 1T phase MoS2 nanosheets as supercapacitor electrode materials 10 (2015) 313–318.

[29] Z. Du, S. Yang, S. Li, J. Lou, S. Zhang, S. Wang, B. Li, Y. Gong, L. Song, X. Zou, P. M. Ajayan, Conversion of non-van der Waals solids to 2D transition-metal chalcogenides 577 (2020) 492–496.

[30] Y. Wang, Y. Zhu, S. Afshar, M.W. Woo, J. Tang, T. Williams, B. Kong, D. Zhao, H. Wang, C. Selomulya, One-dimensional CoS2-MoS2 nano-flakes decorated MoO2 sub-micro-wires for synergistically enhanced hydrogen evolution 11 (2019) 3500–3505.

[31] M.S. Faber, R. Dziedzic, M.A. Lukowski, N.S. Kaiser, Q. Ding, S. Jin, High-performance electrocatalysis using metallic cobalt pyrite (CoS2) micro- and nanostructures 136 (2014) 10053–10061.

[32] P. Cheng, K. Sun, Y.H. Hu, Memristive behavior and ideal memristor of 1T phase MoS2 nanosheets 16 (2016) 572–576.

[33] J. Zheng, H. Zhang, S. Dong, Y. Liu, C. Tai Nai, H. Suk Shin, H. Young Jeong, B. Liu, K. Ping, High yield exfoliation of two-dimensional chalcogenides using sodium naphthalenide 5 (2014) 2995.

[34] L. Cai, J. He, Q. Liu, T. Yao, L. Chen, W. Yan, F. Hu, Y. Jiang, Y. Zhao, T. Hu, Z. Sun, S. Wei, Vacancy-induced ferromagnetism of MoS2 nanosheets 137 (2015) 2622–2627.

[35] X. Zou, Y. Zhang, Noble metal-free hydrogen evolution catalysts for water splitting 44 (2015) 5148–5180.

[36] F. Ma, Y. Liang, P. Zhou, F. Tong, Z. Wang, P. Wang, Y. Liu, Y. Dai, Z. Zheng, B. Huang, One-step synthesis of Co-doped 1T-MoS2 nanosheets with efficient and stable HER activity in alkaline solutions 244 (2020) 122642.

[37] N.H. Attanayake, L. Dheer, A.C. Thenuwara, S.C. Abeyweera, C. Collins, U. V. Waghmare, D.R. Strongin, Ni- and co-substituted metallic MoS2 for the alkaline hydrogen evolution reaction 7 (2020) 3606–3615.

[38] Y. Cui, X. Tan, K. Xiao, S. Zhao, N.M. Bedford, Y. Liu, Z. Wang, K.H. Wu, J. Pan, W. H. Saputera, S. Cheong, R.D. Tilley, S.C. Smith, J. Yun, L. Dai, R. Amal, D.W. Wang, Tungsten oxide/carbide surface heterojunction catalyst with high hydrogen evolution activity 5 (2020) 3560–3568.

[39] Q. Tang, D.-e Jiang, Mechanism of hydrogen evolution reaction on 1T-MoS2 from first principles 6 (2016) 4953–4961.

[40] S.H. Lin, J.L. Kuo, Activating and tuning basal planes of MoO2, MoS2, and MoSe2 for hydrogen evolution reaction 17 (2015) 29305–29310.

[41] X. Liang, C.-M.L. Wu, Metal-free two-dimensional phosphorus carbide as an efficient electrocatalyst for hydrogen evolution reaction comparable to platinum 71 (2020), 104603.

[42] V.L. Deringer, A.L. Tchougreeff, R. Dronskowski, Crystal orbital hamilton population (COHP) analysis as projected from plane-wave basis sets 115 (2011) 5461–5466.

[43] R. Dronskowski, P.E. Blochl, Crystal orbital hamilton populations (COHP) energy-resolved visualization of chemical bonding in solids based on density-functional calculations 97 (1993) 8617–8624.